

**AJP**

ISSN : 0971 - 3093

Vol 27, Nos 9 -12, September-December 2018

# ASIAN JOURNAL OF PHYSICS

**An International Research Journal**

Advisory Editors : W. Kiefer & FTS Yu



Toshimitsu Asakura

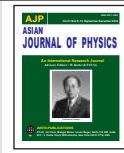


ap

**ANITAPUBLICATIONS**

FF-43, 1st Floor, Mangal Bazar, Laxmi Nagar, Delhi-110 092, India

B O : 2, Pasha Court, Williamsville, New York-14221-1776, USA



## Topographic imaging of skin subsurface bleeding in a recovery process using diffuse reflectance images

Takaaki Maeda<sup>1</sup>, Izumi Nishidate<sup>2</sup>, Tomonori Yuasa<sup>3</sup>, and Yoshihisa Aizu<sup>3</sup>

<sup>1</sup>Kushiro National College of Technology, Kushiro, Hokkaido 084-0916, Japan

<sup>2</sup>Tokyo University of Agriculture and Technology, Tokyo 184-8588, Japan

<sup>3</sup>Muroran Institute of Technology, Muroran, Hokkaido 050-8585, Japan

Dedicated to Prof T Asakura

A method is proposed for measuring the depth and thickness of skin subsurface bleeding using diffuse reflectance images at two isosbestic wavelengths of hemoglobin, 420 and 585 or 800 nm, at which absorbing coefficients of oxy- and deoxy-hemoglobin have the same value. Monte Carlo simulation is used to investigate characteristic curves of the absorbance versus depth or thickness. These curves are formulated by exponential approximation which is adaptive to individual variations of melanin in epidermis and hemoglobin in dermis. Experiments with skin tissue phantoms were carried out to show the ability of the method. The method is capable for measuring the depth smaller than 700-800  $\mu\text{m}$  and the thickness smaller than 350-400  $\mu\text{m}$  in blood concentration lower than about 20 %. By this ability, the method was successfully applied to topographic imaging of the internal bleeding in skin subsurface tissue of human forearm, particularly in a recovery process. © Anita Publications. All rights reserved.

**Keywords:** Diffuse reflectance, Skin tissue, Absorbance, Isosbestic wavelengths

### 1 Introduction

Depth and thickness of a local blood region in skin tissue are one of important parameters and should be known for diagnostics and therapeutics in dermatology. Laser treatments of cutaneous hypervascular malformations such as port-wine stain birthmarks require information of the depth and thickness for optimizing pulse duration and radiant exposure [1,2]. Diagnosing of internal bleeding or hemorrhage and cancerous regions in skin tissue can be reliably performed on the basis of depth and thickness measurements. For this purpose, several non-invasive techniques have been reported including ultrasound [3], photoacoustic [4,5], and photothermal [6] methods. The ultrasound method is effective for probing deep regions in tissue, but suffers from insufficient resolution especially for skin surface regions. The photoacoustic and photothermal methods are able to provide reasonable resolution ( $\sim 100 \mu\text{m}$ ) and probing depth (several mm), but they need use of a pulsed laser source, and are inconvenient for routine clinical uses. Techniques such as optical coherence tomography [7, 8] and confocal microscopy [9] are useful for imaging with high resolution, regions in depth up to about 2 mm and 200  $\mu\text{m}$ , respectively. However, they are mainly based on light scattering at the tissue boundaries and, thus, less effective for highly absorbing regions such as bloody portions. For diagnosing internal bleeding particularly in the fields of surgery or post-surgery bleeding, a fluorescence technique was developed [10], but the use of fluorescence is undesirable for daily applications due to toxic risk.

Jacques *et al* [11] reported a diffuse reflectance method which measures the average depth of capillary networks in dermis using two isosbestic wavelengths of hemoglobin, at which the absorbing coefficients

---

Corresponding author :

e-mail: [aizu@mmm.muroran-it.ac.jp](mailto:aizu@mmm.muroran-it.ac.jp) (Yoshihisa Aizu)

of oxy- and deoxy-hemoglobin have the same value. This method provided measurements independent of oxygenation, but did not consider influence of variation in melanin concentration among subjects. Nishidate *et al* [12, 13] presented a method for imaging the depth and thickness of venous blood vessels in human forearm skin tissue, using the isosbestic wavelengths of hemoglobin, 420, 585, and 800 nm. This method enabled compensation for variations in melanin concentration in epidermis and hemoglobin concentration in dermis. Through numerical and experimental investigations, the depth was estimated in a range of 1.5-3.0 mm and the thickness was of 0.25-1.5 mm, providing that the venous blood vessels were filled with 100-% concentration of blood with hematocrit of 44 %. The results were also successfully compared with those obtained by an ultrasound imaging method, demonstrating good correlation between the two methods. Thus, this method may be applicable to internal bleeding if the bleeding depth, thickness and blood concentration meet the ranges and conditions mentioned above, respectively. A possible example may be vascular lesions.

In this paper, we treat another type of internal bleeding which possibly occurs just under the epidermis-dermis junction in the upper dermis. In this case, the depth and thickness may take ranges smaller than several hundred microns, and smaller than a few hundred microns, respectively. The blood concentration in this bleeding seems to be substantially low due to blood leakage from capillary network. This type of bleeding cannot be probed by the previous method [13], which is based on the ratio of absorbance values at two different wavelengths. Here, we propose a new approach for measuring the depth and thickness of skin subsurface bleeding by using the similar analogy to the previous method but on the basis of a single absorbance curve at isosbestic wavelength. Monte Carlo simulation was used to investigate characteristic curves of the absorbance versus depth and thickness, and to formulate the relations by exponential approximation. Experiments with skin tissue phantoms were carried out to verify validity of the proposed approach. The present approach enables us to measure the depth smaller than 700-800  $\mu\text{m}$  and the thickness smaller than 350-400  $\mu\text{m}$  of bleeding in blood concentration lower than about 20 %. Thus, this ability makes it possible to monitor quantitatively the recovery process in which the bleeding becomes thinner and thinner with substantially decreasing blood concentration. Use of imaging modality provides 3-D topographic monitoring of the internal bleeding in a forearm skin tissue in a recovery process.

## 2 Skin subsurface bleeding

### 2.1 Assumption for a bleeding region

Human skin consists of different types of tissues and vessels or capillaries in complex structure. The skin tissue is roughly divided into three main layers, epidermis, dermis, and subcutaneous fat layer. Describing the skin tissue structure in more detail, epidermis represents stratum corneum, stratum granulosum, stratum spinosum, and stratum basale. Dermis consists of several sub-layers such as papillary dermis, subpapillary dermis, and reticular dermis. Epidermis is mainly made out of melanin, while dermis contains hemoglobin in blood within the superficial plexus. This plexus exists mainly in papillary and subpapillary dermis in depth of typically 100-400  $\mu\text{m}$  [14-16]. The shallowest capillary networks under the epidermis-dermis junction distributes within papillary dermis in thickness typically less than 100  $\mu\text{m}$  [14-16]. Internal bleeding treated here is a type caused possibly by external force on the skin surface, such as pressure or suction. The bleeding in this case is probably due to blood leakage by destruction of capillary vessels in papillary and/or subpapillary dermis. On the other hand, the reticular dermis is typically in the region of 400-1600  $\mu\text{m}$  in depth [14-16] and includes some amount of hemoglobin, thus has less contribution to the bleeding of interest here. From these anatomical considerations, the internal bleeding focused in this study is assumed to have depth less than several hundred microns and thickness less than a few hundred microns. The bleeding is considered as a result from blood leakage and diffusion into the surrounding tissue. Thus blood concentration in this type of bleeding is assumed to be substantially low in comparison of that inside blood vessels.

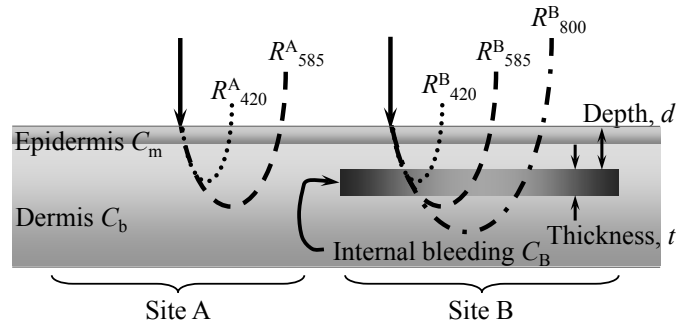


**Fig 1.** Layered skin tissue model and reflection of light at wavelengths 420, 585, and 800 nm. Site A indicates the common skin region and site B includes internal bleeding.  $C_m$  is melanin concentration in epidermis,  $C_b$  is hemoglobin concentration in dermis, and  $C_B$  is that in the bleeding.

## 2.2 Layered skin tissue model

For studies aimed at light transport, a simple layered model is often used under reasonable approximation [14]. In this study, we employ a two-layered model consisting of epidermis and dermis shown in Fig 1. The model contains two sites A and B, and the latter includes a local blood region having depth  $d$  and thickness  $t$  in dermis as an internal bleeding. The two sites A and B are assumed to be neighbor with each other and to have the same optical properties both in epidermis and dermis, except for the bleeding region. Three notations  $C_m$ ,  $C_b$ , and  $C_B$  indicate concentrations of melanin in epidermis, hemoglobin in dermis, and that in the bleeding, respectively. For convenience, it is assumed that melanin and hemoglobin are distributed homogeneously over the epidermis, and each of the dermis and bleeding, respectively. Subcutaneous fat layer under dermis is omitted since light re-emitted from the skin surface is almost contributed by scattering in epidermis and dermis.

## 3 Principle

### 3.1 Simulated properties of absorbance

To determine the depth and thickness of bleeding from diffuse reflectance measurements, we first pay attention to relations of the absorbance versus depth or thickness at the three isosbestic wavelengths of 420, 585, and 800 nm, following the previous principle [13]. As seen from Fig 1, light incident on site B penetrates into the internal bleeding. Thus, diffuse reflectance  $R^B_\lambda$  in which  $\lambda$  is wavelength may depend on the depth  $d$  and thickness  $t$ . To investigate the relations, we use the Monte Carlo simulation [17]. In the simulation, the diffuse reflectance  $R^B_\lambda$  can be calculated from multi-layered skin tissue model such as Fig 1. Executing the simulation code [17] requires input values of a thickness of each layer and the four optical parameters of each layer at each wavelength: scattering coefficient  $\mu_s$ , absorption coefficient  $\mu_a$ , anisotropy factor  $g$ , and refractive index  $n$ . According to the previous study [13], we use typical values published in literatures [14-16, 18-27]. The absorption coefficients of epidermis, dermis, and bleeding region are given by specifying volume concentrations  $C_m$ ,  $C_b$ , and  $C_B$  of melanin in epidermis, hemoglobin in dermis, and that in the bleeding, respectively using a relation of  $\mu_a = \epsilon C$  ( $\epsilon$  and  $C$  are molar extinction coefficient and concentration of chromophore). The hematocrit of blood is assumed to be 44 %, which corresponds to the hemoglobin concentration in blood of about 150 g/l. A situation in which a volume is fully filled with this blood is assumed to be 100 % for  $C_b$  and  $C_B$ . Refractive index  $n$  for each layer is assumed to be 1.4 at the three wavelengths. Thickness values were set to be 60  $\mu\text{m}$  and 4.94 mm for epidermis and dermis, respectively. The depth and thickness of the bleeding were ranged in 60  $\mu\text{m}$  – 1.0 mm and 20  $\mu\text{m}$  – 1.0 mm, respectively. The other values used for the simulation are shown in Table 1. Values of  $\mu_a$  in Table 1 correspond to  $C_m = 5\%$  in epidermis,  $C_b = 0.4\%$  in dermis, and  $C_B = 47\%$  in bleeding, respectively, as a typical example. Note that

the absorption coefficient  $\mu_a$  used here is independent of the oxygenation of blood since the present method uses light at isosbestic wavelengths. One sample of reflectance  $R_{\lambda}^B$  was calculated with 100,000 number of photons and threshold of 0.001 for photon traveling in the Wang's code [17] of Monte Carlo simulation. The resultant reflectance  $R_{\lambda}^B$  was converted to absorbance  $OD_{\lambda}^B$  by  $OD_{\lambda}^B = -\log_{10} R_{\lambda}^B$ .

**Table 1.** Optical parameters  $\mu_a$ ,  $\mu_s$ , and  $g$  of each layer in human skin tissue at the three wavelengths.

	Optical parameter	Wavelength (nm)		
		420	585	800
Epidermis	$\mu_a$ (cm <sup>-1</sup> )	59.71	20.24	3.59
	$\mu_s$ (cm <sup>-1</sup> )	334.23	148.86	93.02
	$g$	0.74	0.79	0.85
Dermis	$\mu_a$ (cm <sup>-1</sup> )	9.22	0.73	0.02
	$\mu_s$ (cm <sup>-1</sup> )	334.23	148.86	93.02
	$g$	0.74	0.79	0.85
Bleeding	$\mu_a$ (cm <sup>-1</sup> )	461.21	36.70	0.85
	$\mu_s$ (cm <sup>-1</sup> )	579.07	836.16	752.61
	$g$	0.97	0.98	0.98

Figures 2(a) and 2(b) show typical variations of  $OD_{\lambda}^B$  at the three wavelengths versus depth and thickness, respectively, simulated on the above conditions.  $OD_{420}^B$  and  $OD_{585}^B$  decrease for increasing depth up to about 0.4 mm and 1.0 mm, respectively, while  $OD_{800}^B$  shows low absorbance and remains unchanged with the depth. Absorption of light by hemoglobin is low at 800 nm in comparison with those at 420 and 585 nm, and the light penetrates into the deeper region than that of the blood layer treated in this study. Thus,  $OD_{800}^B$  is independent of the depth in its range of 0 - 1.0 mm. This property at 800 nm is clearly different from the case treated in the previous method [13], and is specific to the internal bleeding having small depth and thickness with low hemoglobin concentration. In Fig 2(b),  $OD_{420}^B$  shows no dependency on the thickness and  $OD_{800}^B$  increases gradually with the thickness, while  $OD_{585}^B$  increases largely up to about 0.4 mm in thickness. The latter characteristic for  $\lambda = 585$  nm is also clearly different from the case presented in the previous method [13]. Light of 420 nm is highly absorbed by hemoglobin in skin tissue and hardly passes through the blood layer, thus  $OD_{420}^B$  is large and insensitive to a change of the thickness. Conversely, light of 800 nm substantially passes through the blood layer in the forward and backward directions and, thus,  $OD_{800}^B$  is small and weakly dependent on the thickness. Light of 585 nm may penetrate a region in depth comparative with that of the blood layer and, thus,  $OD_{585}^B$  increases very sensitively to increase in thickness. On the basis of these absorbance properties, we decided to employ curves of  $OD_{420}^B$  and  $OD_{585}^B$  for measuring the depth and thickness, respectively in this study. Another possible substitute is  $OD_{585}^B$  for the depth and  $OD_{800}^B$  for the thickness. A ratio of two absorbances is also considered as a promising indication, for example,  $OD_{420}^B/OD_{800}^B$  for the depth and  $OD_{585}^B/OD_{420}^B$  for the thickness. This possibility is at present under study and may be reported in the near future.

### 3.2 Formulation

It should be noted that absorbance curves in Fig 2 are of course just one example specified by input values used in the calculation, and they may vary with different values. According to the previous study [13], the curves for the depth are especially influenced by values of melanin concentration  $C_m$  in epidermis and hemoglobin concentration  $C_b$  in dermis, and the curves for the thickness are also by the depth  $d$  in addition to  $C_m$  and  $C_b$ . Usually values of  $C_m$  and  $C_b$  can be varied depending on individuals, positions, and

occasions. Nishidate *et al* [12, 13] presented a technique of compensating for variations in  $C_m$  and  $C_b$  using measurements of reflectance  $R^A_\lambda$  or absorbance  $OD^A_\lambda$  at  $\lambda = 420$  and  $585$  nm in site A which are free from the internal bleeding as shown in Fig 1. In this technique, the two concentrations  $C_m$  and  $C_b$  are given by two

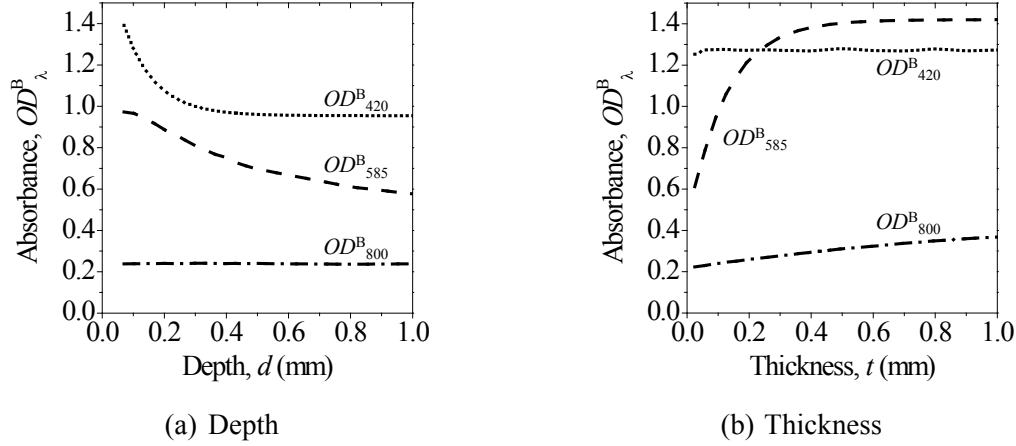


Fig 2(a). Relation of absorbance  $OD^B_\lambda$  and depth  $d$  for thickness  $t = 0.1$  mm and (b) relation of absorbance  $OD^B_\lambda$  and thickness  $t$  for depth  $d = 0.1$  mm, at 420, 585, and 800 nm in wavelength  $\lambda$ .

multiple regression equations as [12, 13]

$$C_m = a_1 \times OD^A_{420} + a_2 \times OD^A_{585} + a_0 \quad (1)$$

$$C_b = b_1 \times OD^A_{420} + b_2 \times OD^A_{585} + b_0 \quad (2)$$

where  $a_i$  and  $b_i$  ( $i = 0, 1, 2$ ) are regression coefficients that have been determined in advance by performing multiple regression analysis of 50 data sets for various values of  $C_m$  and  $C_b$ , and their corresponding results of  $OD^A_{420}$  and  $OD^A_{585}$  obtained by the Monte Carlo simulation. Thus, measurements of  $R^A_{420}$  and  $R^A_{585}$  or  $OD^A_{420}$  and  $OD^A_{585}$  give us estimated values of  $C_m$  and  $C_b$  on every measurement. Equations (1) and (2) hold in ranges of  $C_m = 1$ -10% and  $C_b = 0.2$ -1% in the present study. The previous study indicated that the absorbance curve as shown in Fig 2(a) rises with increasing values of  $C_m$  and/or  $C_b$  [13]. We simulated curves of  $OD^B_{420}$  versus depth for 50 different combinations of  $C_m$  in 1-10% and  $C_b$  in 0.2-1%. By analyzing dependency of those curves on values of  $C_m$  and  $C_b$ , we found that the curves are well approximated by an adaptive exponential function as

$$OD^B_{420} = r_d + A_d \exp\left[-\frac{d}{u_d}\right], \quad (3)$$

where three parameters  $r_d$ ,  $A_d$ , and  $u_d$  are specified adaptively to estimated values of  $C_m$  and  $C_b$  by

$$\begin{pmatrix} r_d \\ A_d \\ u_d \end{pmatrix} = \begin{pmatrix} \alpha_0 & \alpha_1 & \alpha_2 \\ \beta_0 & \beta_1 & \beta_2 \\ \gamma_0 & \gamma_1 & \gamma_2 \end{pmatrix} \begin{pmatrix} 1 \\ C_m \\ C_b \end{pmatrix}. \quad (4)$$

In Eq (4),  $\alpha_i$ ,  $\beta_i$ , and  $\gamma_i$  ( $i = 0, 1, 2$ ) are regression coefficients that have been obtained in advance by multiple regression analysis of 50 data sets for given values of  $C_m$  and  $C_b$ , and the corresponding results of  $OD^B_{420}$  simulated by the Monte Carlo method. Thus, the depth  $d$  is formulated as

$$d = -u_d \cdot \ln\left[\frac{OD^B_{420} - r_d}{A_d}\right], \quad (5)$$

which indicates that the depth  $d$  can be determined by measuring  $OD_{420}^B$ , together with  $OD_{420}^A$  and  $OD_{585}^A$ . Equations (3) and (4) mean that the approximation to the curve of  $OD_{420}^B$  versus depth can be adaptive to values of  $C_m$  and  $C_b$  estimated on every measurement and, thus, Eq (5) can be adaptive to  $C_m$  and  $C_b$  as well.

In the same way with the depth, we next simulated curves of  $OD_{585}^B$  versus thickness and analyzed the dependency on values of  $C_m$ ,  $C_b$ , and  $d$ . Then, we approximated the curves by an exponential function as

$$OD_{585}^B = r_t + A_t \exp\left[-\frac{t}{u_t}\right], \quad (6)$$

where  $r_t$ ,  $A_t$ , and  $u_t$  are specified by

$$\begin{pmatrix} r_t \\ A_t \\ u_t \end{pmatrix} = \begin{pmatrix} \delta_0 & \delta_1 & \delta_2 & \delta_3 \\ \phi_0 & \phi_1 & \phi_2 & \phi_3 \\ \sigma_0 & \sigma_1 & \sigma_2 & \sigma_3 \end{pmatrix} \begin{pmatrix} 1 \\ C_m \\ C_b \\ d \end{pmatrix}. \quad (7)$$

In Eq (7),  $\delta_i$ ,  $\phi_i$ , and  $\sigma_i$  ( $i = 0, 1, 2, 3$ ) are regression coefficients obtained in the same way as in Eq (4), but here the data sets were prepared for given values of  $C_m$ ,  $C_b$ , and  $d$  and the corresponding results of  $OD_{585}^B$ . Thus, the thickness  $t$  is formulated as

$$t = -u_t \cdot \ln\left[\frac{OD_{585}^B - r_t}{A_t}\right], \quad (8)$$

and can be determined by use of measured values of  $OD_{585}^B$ , together with  $OD_{420}^A$  and  $OD_{585}^A$ . Equation (7) indicates that, specifying of  $r_t$ ,  $A_t$ , and  $u_t$  requires values of the depth  $d$  in addition to  $C_m$  and  $C_b$ . The depth  $d$  is determined by Eq (5) before determination of the thickness  $t$ .

The absorbances  $OD_{\lambda}^A$  and  $OD_{\lambda}^B$  may also depend on the other factors such as scattering coefficient  $\mu_s$ , anisotropy factor  $g$ , and refractive index  $n$ . These should be known for reliable determination of the depth and thickness. However, it has not been realized yet in the present method. Thus, we assume that these factors are given by typical published values. On actual measurements, two sites A and B are easily discriminated by visual observation of internal bleeding in images. The values  $OD_{\lambda}^A$  and  $OD_{\lambda}^B$  in the sites A and B, respectively, are obtained simultaneously from one reflectance image which covers both A and B sites. It should be noted that regression coefficients in Eqs (4) and (7) are available in the ranges of  $d = 60\mu\text{m}-1.0\text{mm}$  and  $t = 20\mu\text{m}-1.0\text{mm}$  and, thus, Eqs (5) and (8) hold in these ranges in the present study.

## 4 Experiments

### 4.1 Measuring system

A measuring system is shown in Fig 3. White light from a 150W halogen lamp illuminates a target area of an object via a light guide, ring illuminator, and polarizer. Light reflected from the object is acquired with a 16-bit cooled CCD camera via an interference filter, polarizer, and imaging lens. A set of these two polarizers are arranged in a cross-polarization direction with each other to suppress the specular reflection from the object surface. In the previous studies [12, 13], we employed illumination of oblique incidence. This scheme was different from the geometry assumed in MC simulation which was performed to derive regression coefficients. The difference was supposed to be a source of measurement errors [28, 29], since the obliquely incident illumination may specify a region of depth different from that with the normal incidence. To overcome this problem, we introduced a ring illuminator which enables us to put the illumination and imaging optics in a co-axial arrangement almost normal to the object surface. Three interference filters of 420, 585, and 800 nm wavelengths having 10 nm FWHM are replaced one by one and, thus, three images are obtained in order. These images are converted to reflectance images  $R_{\lambda}$  by referencing to responses of dark current noise and a white standard which have been acquired beforehand.

Reflectance images  $R_\lambda$  of an object surface over a blood layer (site B) and its surrounding area (site A) are then converted to optical density or absorbance images  $OD_\lambda$ . The two sites A and B are visually recognized on the reflectance images. Then, the two absorbance values  $OD_{420}^A$  and  $OD_{585}^A$  are obtained by averaging the image data sampled in a certain area of site A, and used to calculate the melanin concentration  $C_m$  in the epidermis and the blood concentration  $C_b$  in the dermis, by using Eqs (1) and (2). By substituting the obtained values of  $C_m$  and  $C_b$  into Eq (4), the parameters  $r_d$ ,  $A_d$ , and  $u_d$  are specified and the Eq (5) is then specified. The two other absorbance values  $OD_{420}^B$  and  $OD_{585}^B$  in site B are obtained in the same way with  $OD_{420}^A$  and  $OD_{585}^A$ . By use of the  $OD_{420}^B$ -value in Eq (5), the depth  $d$  is determined and pixel-by-pixel analysis gives the 2-D distribution of depth values. By substituting the determined values of depth  $d$  together with  $C_m$  and  $C_b$  into Eq (7), the parameters  $r_b$ ,  $A_b$ , and  $u_b$  and, thus, the Eq (8) are specified. A use of the  $OD_{585}^B$ -value in Eq (8) gives the thickness  $t$  and finally forms the 2-D distribution of thickness values.

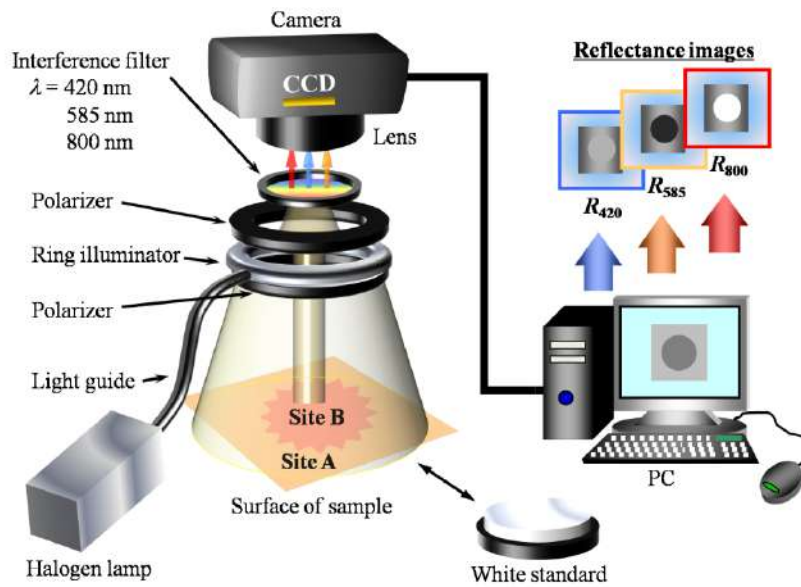


Fig 3. Apparatus for acquisition of reflectance images.

#### 4.2 Phantom measurements

Figure 4 shows schematically construction of a tissue-like agar gel phantom which we have developed in the previous study [13], including two photographs of a cross section and top surface. The details about preparation of phantoms can be referenced in our article [13]. The phantom with an area of  $26\text{mm} \times 76\text{mm}$  consists of four component layers as shown in Fig 4. The top layer  $L_1$  corresponds to epidermis containing coffee solution with a specified concentration  $C_c$  as a substitute of melanin having  $C_m$ . The second to fourth layers  $L_2$ ,  $L_3$ , and  $L_4$  correspond to the upper, middle, and lower regions of dermis, respectively, containing a small amount of fully-oxygenated horse blood,  $C_b$ , for substituting blood content in capillary network. These four layers include also Intralipid 10% to characterize a scattering condition. As shown in Fig 4, a circular part (diameter of 15 mm) in the center of the third layer  $L_3$  was cut out and, then, replaced with a circular blood inclusion of concentration  $C_B$  in the same form. The depth  $d$  of this blood inclusion was defined hereby as the total thickness of the first and second layers  $L_1$  and  $L_2$ , while the thickness  $t$  of the blood inclusion was the same with that of the third layer  $L_3$ . All the layers were piled to be a multi-layered phantom and, finally, set between two glass slides for handling and measurements. The hematocrit of blood used here was regulated to be 20%. Values of  $C_c$  and  $C_b$  were set to be 5% and 0.4%, respectively.

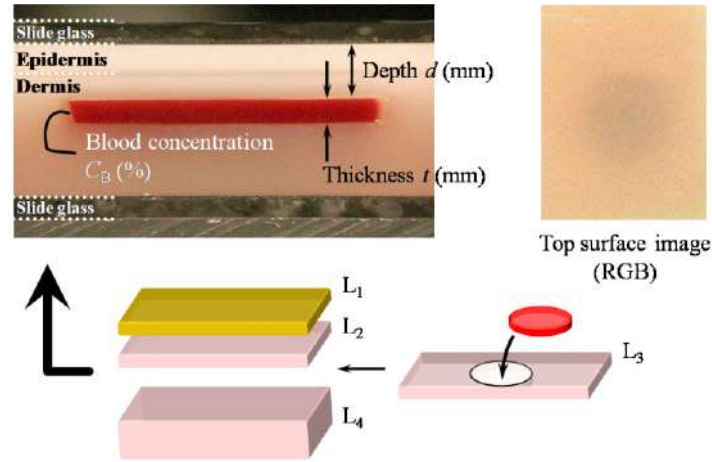


Fig 4. Construction of a tissue-like agar gel phantom including a circular internal bleeding model and two photographs of a cross section and top surface.

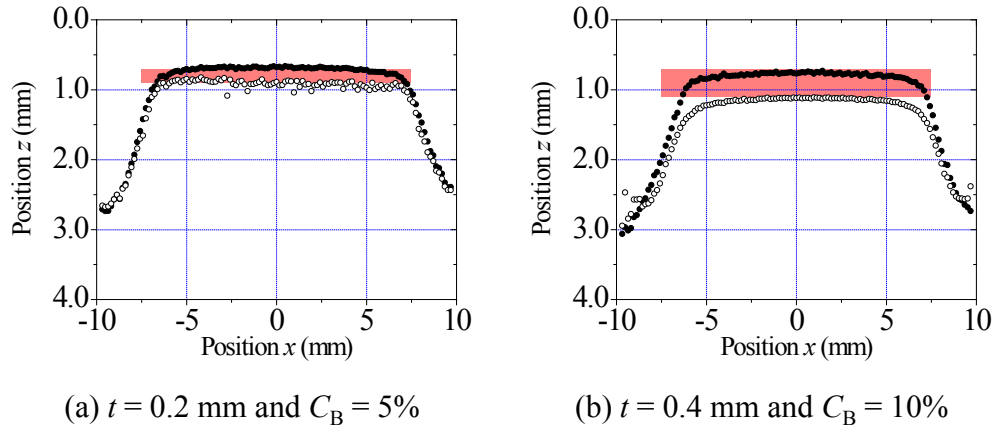


Fig 5. Results of depth and depth-plus-thickness plots in (a)  $d = 0.7\text{mm}$ ,  $t = 0.2\text{mm}$ , and  $C_B = 5\%$  and (b)  $d = 0.7\text{mm}$ ,  $t = 0.4\text{mm}$ , and  $C_B = 10\%$ , along  $x$ -axis at  $y = 0$ . The shaded portion indicates the actual position of the blood inclusion arranged in the phantom.

Figure 5 shows cross-sectional profiles along  $x$ -axis at  $y = 0$ , obtained for two examples of the blood inclusion (a)  $d = 0.7\text{mm}$ ,  $t = 0.2\text{mm}$ , and  $C_B = 5\%$  and (b)  $d = 0.7\text{mm}$ ,  $t = 0.4\text{mm}$ , and  $C_B = 10\%$ . The shaded portion in the figure indicates the position in which the blood inclusion was actually arranged. Measured positions of the upper and bottom surfaces of the inclusion are depicted by plots “●” and “○” obtained from results of the depth and depth-plus-thickness, respectively. The measured profile well agree with the actual cross section in Fig 5(a). The blurred effect is found near the blood inclusion edge, which is mainly due to diffusion of light in the phantom containing Intralipid 10%. In Fig 5(b), results demonstrate a good agreement with the actual position in the center of the blood inclusion (around  $x = 0$ ), while errors are increased in the outer area of the inclusion ( $|x| > 4\text{mm}$ ). This is due to the values in the thickness and concentration of the blood inclusion in Fig 5(b) which was larger than those in Fig 5(a). The values of  $d = 0.7 \text{ mm}$  and  $t = 0.4\text{mm}$  used in experiment of Fig 5(b) were probably close to the maximum of measurable ranges of  $d$  and  $t$ . Therefore, the results in Figs 5(a) and 5(b) indicate that the new approach proposed in this study is useful for measuring the depth and thickness of the blood inclusion in the specific range, less than hundred microns and a few hundred microns, respectively, with the lower blood concentration, as assumed in Fig 5.

### 4.3 Measurements on human forearm

To investigate the usefulness of the proposed approach for *in-vivo* measurements, we next carried out experiments for internal bleeding in human forearm skin. We caused internal bleeding in right forearm skin tissue of a healthy adult male (24 years old) under informed consent, by using suction with a safely-cut needle tube as shown in Fig 6(a). A suction force and period necessary for expected internal bleeding were unknown, so that we tried several times this suction with different levels of force and period by beginning from a sufficiently safe level, gradually increasing this level and observing resultant internal bleeding in several months. Through this experience, we found the safe and meaningful level of force and period for expected internal bleeding. Figures 6(b)-6(e) show photographs of internal bleeding used in this study before, and 24, 48, and 144 hours after the suction. The rectangle area indicates a measured region. The internal bleeding is clearly observed in Fig 6(c), slightly recovered in Fig 6(d), and fairly recovered in Fig 6(e). During this recovery process, the bleeding seems to become thinner, and blood concentration seems to become lower.



(a) Bleeding by suction (b) Before (c) 24 hours (d) 48 hours (e) 144 hours

Fig 6. (a) Internal bleeding caused by the suction, and photograph of forearm (b) before the suction, and (c) 24, (d) 48, and (e) 144 hours after the suction.

As described in Sect. 2.1, internal bleeding caused by the suction on the skin surface mainly results from blood leakage in the shallowest capillary network in papillary dermis under the epidermis-dermis junction. Thus, the bleeding shown in Fig 6 is expected to have the smaller depth, thickness, and blood concentration. To estimate very roughly in advance the supposed ranges of depth, thickness, and blood concentration of the internal bleeding under study, we observed a reflectance image  $R_\lambda$  of the bleeding, 24 hours after the suction, at the three wavelengths. We produced several examples of the phantom having different combinations of depth, thickness, and blood concentration, and their reflectance images  $R_\lambda$  at the three wavelengths as well. Then we compared the reflectance images between the bleeding and the phantoms. Among several phantoms, we found that one having depth  $d = 0.7\text{mm}$ , thickness  $t = 0.2\text{mm}$ , and blood concentration  $C_B = 5\%$  represented considerably close reflectance images at the three wavelengths. Figure 7 demonstrated that those reflectance images visually well agree with each other between the bleeding (I) and phantom (II) at each wavelength. Of course, the condition of light scattering and absorption is different between the human forearm skin and artificial phantom. Thus, the values of  $d$ ,  $t$ , and  $C_B$  in the phantom example of Fig 7 cannot directly be applied to estimation of those in the bleeding in a human forearm of Fig 7. However, their visual aspects of reflectance show fairly good agreement in combination of the three wavelengths. The reflectance image in Fig 7(a) indicates that the blood region absorbs strongly light of 420 nm. This phenomenon is somewhat reduced at 585 nm in Fig 7(b), and the absorption seems to be substantially weak at 800 nm in Fig 7(c). The penetration depth of light into the human tissue is, in general, 1 mm or so in wavelength around 400 nm, increased with wavelength, and reaches 2~3 mm in that around 800 nm. From this observation, the internal bleeding caused here is supposed to have probably the smaller depth, thickness, and blood concentration than the local blood layers or veins treated in the previous study [13] and, therefore, this sample is considered reasonable for the purpose of the present study.

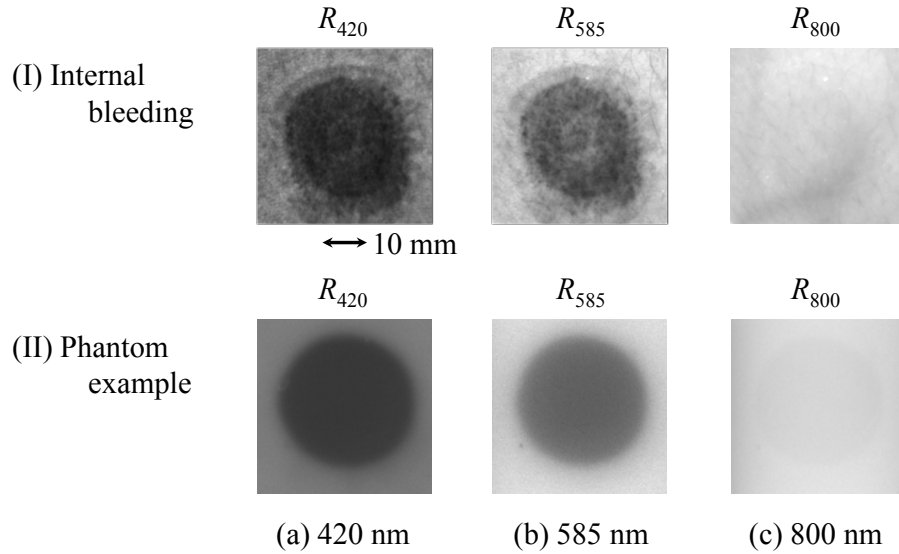


Fig 7. Reflectance images of (I) internal bleeding 24 hours after the suction and (II) a phantom example having a blood inclusion of  $d = 0.7\text{mm}$ ,  $t = 0.2\text{mm}$ , and  $C_B = 5\%$ , at the three wavelengths 420, 585, and 800 nm.

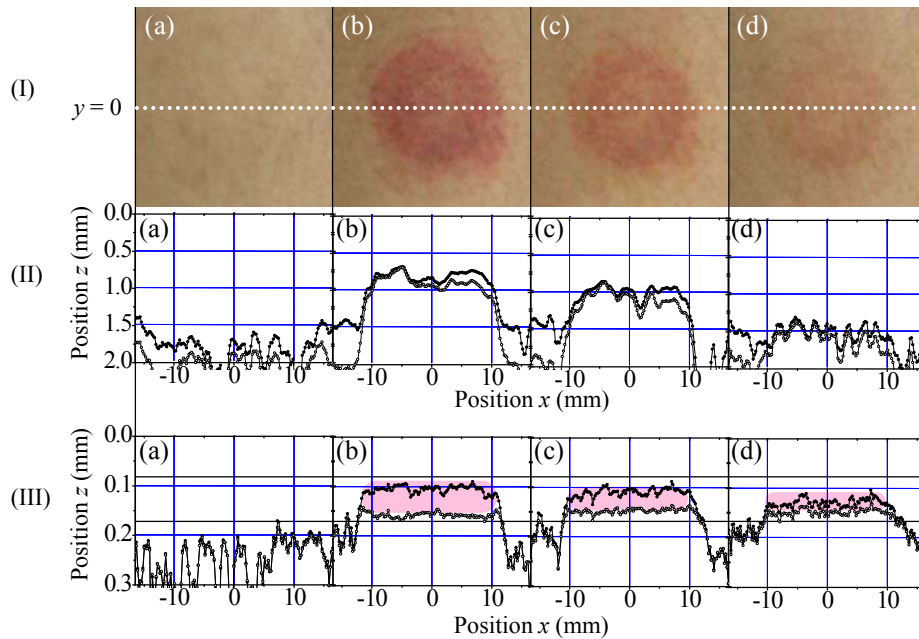


Fig 8. (I) Photographs of the internal bleeding region on skin surface, (II) cross-sectional profiles along  $x$ -axis at  $y = 0$ , obtained by the previous method [13], and (III) those profiles by the present approach, (a) before suction, and (b) 24, (c) 48, and (d) 144 hours after the suction.

Figure 8 shows (I) photographs of the internal bleeding region, (II) cross-sectional profiles along  $x$ -axis at  $y = 0$  obtained by the previous method [13], and (III) those profiles by the present approach. The results in Figs 8(a)-8(d) were obtained in the four different times which correspond to those in Figs 6(b)-6(e)

, respectively. Plots of “●” and “○” show measured profiles of the depth and depth-plus-thickness values and, thus, are supposed to give the profiles of top and bottom surfaces of the bleeding, respectively. The recovery process of the bleeding found in the photos of Fig. 8(I) is hardly extracted in Fig. 8(II) but successfully measured in Fig 8(III). The profile in Fig. 8(II) indicates that the depth is around 750  $\mu\text{m}$  in Fig. 8(II)(b) and increased to about 1 mm in Fig 8(II)(c) and to 1.5 mm in Fig 8(II)(d), and also the thickness is partly lost within each profile of Figs 8(II)(b)-8(II)(d). The part in which the top and bottom surfaces take the same position on  $z$ -axis or the part in which the thickness is lost should mean no bleeding, but the corresponding region in Fig 8(I) is clearly seen to be the bleeding. Thus, the results in Fig 8(II) are quite questionable and look erroneous. This means that subsurface bleeding in skin tissue cannot be probed by the previous method [13]. In Fig 8(III), the upper position of the bleeding is roughly estimated to be 100  $\mu\text{m}$ , 110  $\mu\text{m}$ , and 130  $\mu\text{m}$  on the average in (b), (c), and (d), respectively. The lower position seems to be about 160  $\mu\text{m}$ , 150  $\mu\text{m}$ , and 150  $\mu\text{m}$  in (b), (c), and (d), respectively. The shaded result in Fig 8(III) indicates a region in which the bleeding was probably supposed to exist on the basis of the measured profile. This means that the bleeding becomes thinner with passage of time, without changing its central position on  $z$ -axis. In comparison with Fig 8(II), the result of Fig 8(III) is reasonable with respect to anatomical knowledge on bleeding and its natural recovery. Therefore, we consider that the proposed approach is promising for measuring the position of internal bleeding in skin subsurface tissue.

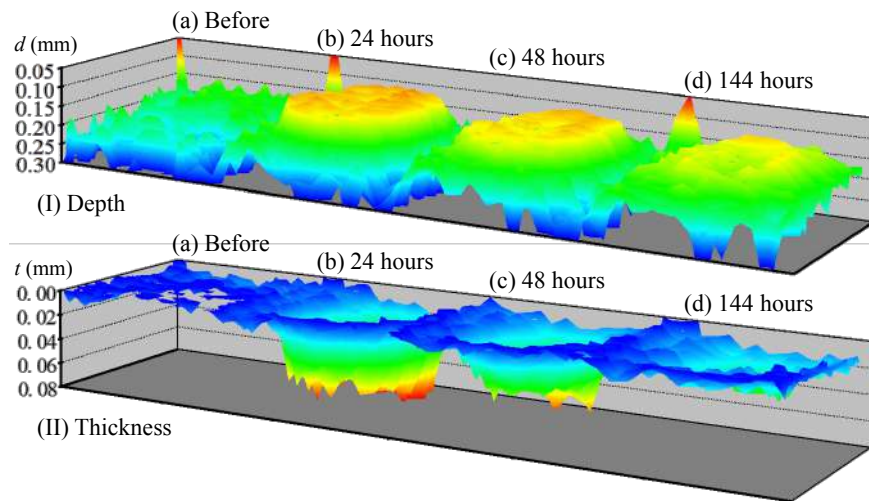


Fig 9. Topographic images of (I) the depth and (II) thickness of the internal bleeding in the recovery process, (a) before the suction, and (b) 24, (c) 48, and (d) 144 hours after the suction.

Figure 9 shows topographic demonstration of the internal bleeding reconstructed by using measured data of the depth and thickness in two dimensions. The passage of time from (a) to (d) in Fig 9 is the same as that in Fig 8. The topographic images successfully present a recovery process of the internal bleeding in a visual manner. In general recovery processes, internal bleeding becomes thinner with passage of time and finally disappears. Thus, monitoring of the recovery process particularly requires the ability of measuring the thickness in a range from near zero to a few hundred microns. According to the simulated result of Fig 2(b), the absorbance  $OD_{585}^B$  increase with change of thickness  $t$  in a range of about 10  $\mu\text{m}$  - 400  $\mu\text{m}$ . Actually, the results of Fig 8(III)(d) and Fig. 9(d) successfully demonstrate the position of even considerably recovered bleeding, though it is unclearly seen in the corresponding photograph of Fig. 6(e) or Fig 8(I)(d). Therefore, the present approach is useful for quantitative monitoring of the recovery process of subsurface bleeding in skin tissue.

There could be a problem to be discussed in determination of the depth and thickness. Their absolute values are determined by Eqs (5) and (8). The two equations contain three adapting parameters  $r_j$ ,  $A_j$ , and  $u_j$  ( $j = d$  or  $t$ ) which are specified with regression coefficients. These regression coefficients have been obtained in advance by assuming that the optical parameters necessary for Monte Carlo simulation take typical values published in literatures [14-16, 18-27]. However, the optical parameters are essentially variable in individual human subjects. Possible deviation from the published values in each of the optical parameters may cause somewhat different result for the depth and thickness. Even if this occurs, the resultant depth and thickness involve only some bias in their values, evenly during the recovery process. Thus, the quantitative monitoring of the bleeding recovery is considered to be available for individual human subjects. During the recovery process, the blood oxygenation state is naturally considered to vary and to be different in each stage of the recovery. In spite of this, the present approach is available because the method uses light at the isosbestic wavelengths where the absorbance is independent of oxygenation in the same way as the previous method [13]. This is the advantage of the present approach for quantitative monitoring of the bleeding recovery.

## 5 Conclusion

The new approach was presented for measuring the depth and thickness of internal bleeding in skin subsurface tissue using the reflectance images at two isosbestic wavelengths of hemoglobin, 420 and 585 nm. Formulation was made for determination of the depth and thickness in the exponential functions which are adaptive to change in concentrations of melanin and hemoglobin in individual skin tissue under measurements. The experimental results confirmed that the present approach was useful for imaging topographically and evaluating quantitatively the skin subsurface bleeding in the recovery process. The approach is expected to probe non-invasively internal bleeding or hemorrhage and cancerous regions in skin subsurface tissue. We intend to clarify measurement accuracy and spatial resolution both in depth and in plane in the next stage of our study.

## Acknowledgment

Part of this work was supported by Grant-in-Aid for Scientific Research from the Japan Society for the Promotion of Science.

## References

1. Verkrusysse W J, Pickering W, Beek J F, Keijzer M, van Gemert M J C, *Appl Opt*, 32(1993)393-398
2. Tunnell J W, Wang L V, Anbari B, *Appl Opt*, 42 (2003)1367-1378
3. Cunitz B W, Kaczkowski P J, Brayman A A, *J Acoust Soc Am*, 117(2005)2584
4. Payne B P, Venugopalan V, Mikić B B, Nishioka N S, *J Biomed Opt*, 8(2003)273-280
5. Viator J A, Choi B, Ambrose M, Nelson J S, Spanier J, *Appl Opt*, 42(2003)3215-3224
6. Li B, Majaron B, Viator J A, Milner T E, Chen Z, Zhao Y, Ren H, Nelson J S, *J Biomed Opt*, 9(2004)961-966; doi.org/10.1117/1.1784470
7. Brezinski M E, Fujimoto J G, *IEEE J Selected Topics in Quantum Electronics*, 5(1999)1185-1192
8. Schmitt J M, Yadlowsky M J, Bonner R F, *Dermatology*, 191(1995)93-98.
9. Rajadhyaksha M, Gonzalez S, Zavislan J M, Anderson R R, Webb R H, *J Invest Dermatol*, 113 (1999)293-303.
10. Ho W Z, Wang F-N, Suh B Y, US Patent application 20050065436, A1 (2005)
11. Jacques S L, Saidil S, Tittel F K, *Proc SPIE*, 2128 (1994)231-237
12. Nishidate I, Aizu Y, Mishina H, *Opt Lett*, 30 (2005)2128-2130
13. Nishidate I, Maeda T, Aizu Y, Niizeki K, *J Biomed Opt*, 12(2007) 054006; doi.org/10.1117/1.2798703
14. Tuchin V V, *Tissue Optics: Light Scattering Methods and Instruments for Medical Diagnosis*, (SPIE-The International Society for Optical Engineering, Washington DC), 2000

15. Meglinski I V, Matcher S J, *Comput Methods Programs Biomed*, 70(2003)179-186.
16. Agache P, Humbert P, (eds) , *Measuring the Skin*, (Springer, Berlin Heidelberg), 2004
17. Wang L H, Jacques S L, Zheng L Q, *Comput Methods Programs Biomed*, 47(1995)131-146
18. Jacques S L, McAuliffe D J, *Photochem Photobiol*, 53(1991)769-775
19. Roggan A, Friebel M, Dörschel K, Hahn A, Muller G, *J Biomed Opt*, 4(1999)36-46
20. van Gemert M J C, Jacques S L, Sterenborg H J C M, Star W M, *IEEE Trans Biomed Eng*, 36(1989)1146-1154
21. Dai T, Pikkula B M, Wang L V, Anvari B, *Phys Med Biol*, 49 (2004)4861-4877
22. Cheong W-F, Prahl S A, Welch A J, *IEEE J Quantum Electr*, 26 (1990)2166-2185.
23. Meglinski I V, Matcher S J, *Physiol Meas*, 23(2002)741-753
24. Churmakov D Y, Meglinski I V, Greenhalgh D A, *J Biomed Opt*, 9(2004)339-346
25. Verkruysse W, Zhang R, Choi B, Aguilar G, Lucassen G, Svaasand L O, Nelson J S, *Phys Med Biol*, 50 (2005)57-70.
26. Zhang R, Verkruysse W, Choi B, Viator J A, Jung B, Svaasand L O, Aguilar G, Nelson J S, *J Biomed Opt*, 10 (2005)024030-11; doi.org/10.1117/1.1891147 .
27. Gambichler T, Matip R, Moussa G, Altmeyer P, Hoffmann K, *J Dermatol Sci*, 44(2006)145-152
28. Pfefer T J, Agrawal A, Drezek R A, *J Biomed Opt*, 10(2005)044016-9; doi.org/10.1117/1.1989308.
29. Wang A M J, Bender J E, Pfefer J, Utzinger U, Drezek R A, *J Biomed Opt*, 10(2005), 044017; doi.org/10.1117/1.1989335

[Received: 17.9.2018; accepted : 1.11.2018]

#### **Izumi Nishidate, Dr. Eng.**

Dr. Izumi Nishidate received the B. Eng, MS Eng., and Dr. Eng. in Mechanical Engineering from Muroran Institute of Technology, in 1999, 2001, and 2004, respectively. From 2004 to 2007, he was a research associate in the Department of Bio-systems Engineering, Yamagata University, Yamagata, Japan. In 2007, he joined the Graduate School of Bio-Applications and Systems Engineering, Tokyo University of Agriculture and Technology, Tokyo, Japan, as an assistant professor, and now he is an associate professor there. His current research activities are in the fields of biomedical optical imaging, biomaterials, bio-systems, and applied optics. He is member of SPIE and some Japanese Societies in the related fields.



#### **Takaaki Maeda, Dr. Eng.**

Dr. Takaaki Maeda received the B. Eng., MS. Eng., and Dr. Eng. in Mechanical Engineering from Muroran Institute of Technology, in 2004, 2006, and 2009, respectively. From 2009 to 2010, he was a post-doctoral researcher in the Optical Instrumentation Laboratory, Muroran Institute of Technology. In 2010, he joined the Mechanical Engineering Department, Kushiro National College of Technology, Hokkaido Japan, as a research associate, and now he is an associate professor there. His current research activities are in the fields of biomedical optical imaging, colorimetry, and spectroscopic measurements. He is member of some Japanese Societies in the related fields.



#### **Yoshihisa AIZU, Dr. Eng.**

Prof Yoshihisa Aizu received Dr. Eng. in electronics from Hokkaido University in 1985. From 1985 to 1989, he was in Kowa Company Limited, Tokyo. In 1989, he joined Hokkaido University as a research associate. From 1990, he was an associate professor at Muroran Institute of Technology, and in 2006 he has been promoted to professor, the position he now holds. From 1992 to 1993, he was a visiting researcher in University Erlangen, Germany. His current research activities are in the fields of biomedical applications of spectroscopy, optical imaging, colorimetry, laser speckle imaging, and laser light scattering. He is a member of SPIE and OSA, and some Japanese Societies in the related fields.



**Tomonori YUASA, Dr. Eng.**

Prof Tomonori Yuasa joined Muroran Institute of Technology as a research associate in 1992. In 2004, he received Dr. Eng. in Mechanical Engineering from Muroran Institute of Technology. From 2006, he was an associate professor at Muroran Institute of Technology. From 1996 to 1997, he was a visiting researcher in Royal Institute of Technology, Sweden, and VTT Information Technology, Finland. His current research activities are in the fields of image processing, colorimetry, database and networking. He is member of some Japanese Societies in the related fields.

e: mail: [yuasa@mmm.muroran-it.ac.jp](mailto:yuasa@mmm.muroran-it.ac.jp)

